

SPECT Lung Delineation via True 3D Active Contours

Alex Wang and Hong Yan, *Fellow, IEEE*

Abstract—In this paper, we developed an automated three-dimensional (3D) lung delineation method that is truly 3D in all aspects capable of handling single photon emission computed tomography (SPECT) lung scans with normal/low maximum count value (MCV) and/or total count value (TCV), defective contours, and/or extraordinary high counts due to hotspots. Four datasets consisting of (1) two sets of 50 randomly selected Monte Carlo simulations and real subjects with normal maximum and/or total count values, and (2) 90 simulations with low MCV and/or TCV and 35 real subjects with similar-ranged MCV/TCV were used as the basis of this study. A fast method was also developed to mass generate simulations with artificial hotspots, and the resulting set of 30 hotspot-infected simulations was also include in our dataset. After removing background noise using dual adaptive exponential thresholding (DUET), 3D Gaussian filter and 3D Sobel kernels are then used for edge enhancement, followed by final contour delineation via 3D active contours. Both quantitative validation and qualitative verification were implemented to evaluate the method. We achieved above 90% congruency overall for both simulations and subject scans that have low/normal MCV/TCV and hotspots.

Index Terms—SPECT lungs, 3D active contours, pulmonary embolism.

I. INTRODUCTION

It has been established that single photon emission computed tomography (SPECT) is an imaging modality favoured over CT and MRI for diagnosing pulmonary embolism (PE) [1] due to its non-invasiveness, high sensitivity and specific nature [2, 3]. As it is critical to obtain accurate lung contours for subsequent PE diagnosis [4, 5], common practice is to use a fixed percentage of the maximum count value (MCV) for thresholding [6-8]. This approach however is subject to the presence of localised high deposition of radioactive agents known as “hotspots”.

Manuscript is a revised/extended work of the following conference paper: A. Wang, and H. Yan, “Delineating SPECT lung contours using 3D snake,” Lecture Notes in Engineering and Computer Science: Proceedings of The International MultiConference of Engineers and Computer Scientists 2010, IMECS 2010, 17-19 March, Hong Kong, vol. 2, pp. 1494-1499, 2010. This work was supported in part by the University of Sydney Postgraduate Award, The University of Sydney, and Norman I. Price Scholarship, School of Electrical and Information Engineering, The University of Sydney.

A. Wang is with the School of Electrical and Information Engineering, The University of Sydney, N.S.W. 2006, Australia (phone: +61 430 306 661; fax: +61 2 9005 5001; e-mail: alexwang80@hotmail.com).

H. Yan is with the Department of Electronic Engineering, City University of Hong Kong, Kowloon, Hong Kong, and also with the School of Electrical and Information Engineering, University of Sydney, Sydney, N.S.W. 2006, Australia (e-mail: h.yan@cityu.edu.hk).

While we have overcome this limitation with our method of dynamic dual exponential thresholding (DUET) which adaptively performs thresholding by examining the 3D volumetric statistical information [9], the method was limited by the lack of spatial considerations, especially with SPECT lung scans that had defective contours due to low MCV and/or total count value (TCV). We later overcame this limitation by combining DUET with traditional planar active contours and achieved above 90% accuracy [10]. However, due to the planar nature of active contouring, each transverse slice rather than the entire volume was processed, losing valuable 3D information such as surface curvature. While preliminary results of implementing 3D active contours continued to be promising [11], we report our findings on the implementation of an automated 3D lung contour delineation method for SPECT scans that is truly 3D in nature in this study.

Since the active contour method was first proposed in 1988 [12], although a lot of research has been carried out into improving the method in terms of speed [13-16], stability [17-19], and convergence [20-24], most of these methods were applied to planar images. While variations of the snake algorithm have been applied to 3D scans of MRI [21, 25-28], CT [29, 30], and other medical imaging modalities [22, 31, 32], they are not truly 3D as the methods were applied on the planar slices before combining and reconstructing the outcome into 3D representations. Although two independent attempts were made to implement active contouring on true 3D images by Jung and Kim [33] and Ahlberg [34] respectively, the former was executing the algorithm on predefined 3D mesh points while the latter was executing the algorithm on MRI images in which the features were well-defined.

II. DATASETS

The same two basic datasets used in our previous studies were used again to evaluate the methods described in this article: 90 SPECT ventilation scans of admitted hospital subjects and 350 Monte Carlo simulations. This ensured data consistency and comparability of results.

Each of the SPECT ventilation scans was acquired using standard protocols. After inhalation of approximately 40MBq of 99mTc-Technegas, data was acquired using a dual/triple-head gamma camera with low-energy high-resolution collimators fitted, and in the format of a 128x128 projection matrix for 120 projection angles. Total acquisition time for the ventilation scan was approximately eight minutes. Finally, the scans were reconstructed using the OSEM block-iterative algorithm with eight subsets and four iterations. 3D Butterworth low-pass filtering with cut-off frequencies of 0.8 cycles/cm at an order of 9.0 was

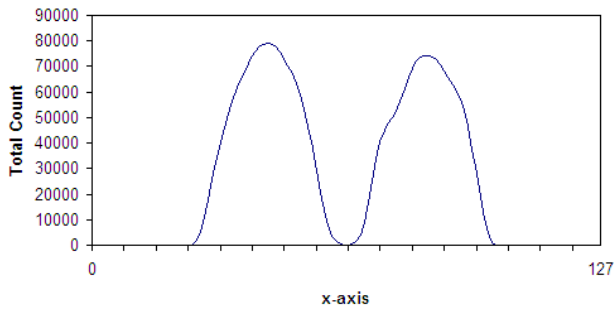


Fig. 1 Sample horizontal topographic representation of a subject SPECT scan. The dividing point identified in this case is $x=62$.

applied without attenuation correction. The resulting reconstructed image set contained 128 slices each measuring 128×128 pixels in size.

A base set of ten gated projections, each consisting of 120 slices measuring 128×128 pixels, was generated using Monte Carlo simulation of photon emission from a phantom with a known volume of 61,660 voxels [35]. This set was then used to build our dataset of 350 hotspot-free, normally ventilated simulations where each simulation is 128×128 pixels in size and contained 128 slices [9].

III. METHOD

A. Pre-processing

We first applied our established method of DUET to remove background noise. While each SPECT lung scan contained the left and right lung and automated extraction of the two lungs via active contouring was desirable [36-38], this was not in scope of this report. The SPECT lung scan was hence divided into the left and right side respectively. A horizontal topographic representation of the scan was created via calculating the total value of each pixel P_{iT} along the x-axis by summing the rows of each image slice for all slices, i.e.,

$$P_{iT} = \sum_{k=0}^n \sum_{j=0}^m P_{ijk} \quad (1)$$

where i, j, k , represent the x-, y-, z-axis, and m, n , represent the number of rows per image slice and total number of image slices respectively. The result contains two peaks that represent the left and right lungs respectively, and the dividing point can be identified as the value with the lowest count, i.e., the valley point. See Fig. 1 for illustration.

B. 3D ROI

Once the lungs are isolated, the initial 3D region of interest (ROI) is established by first identifying the dimension of the 3D box B that encloses the lung. As dynamic thresholding has been applied, the boundaries of B can be easily identified as the maximum and minimum coordinates with non-zero pixel values for each axis, i.e.,

$$x_1, x_2, y_1, y_2, z_1, z_2 \in B \quad (2.1)$$

$$p_{x_1}, p_{x_2}, p_{y_1}, p_{y_2}, p_{z_1}, p_{z_2} > 0 \quad (2.2)$$

$$x_1 > x_2, y_1 > y_2 \text{ and } z_1 > z_2 \quad (2.3)$$

Based on the dimensions identified above and a priori knowledge of the shape of the lung, the initial 3D ROI is best established as a set of discrete ellipsoidal points $R_{ellipse}$ expressed using spherical coordinates such that

$\forall i = 0 \dots (\pi / \phi)$ and $\forall j = 1 \dots (2\pi / \theta)$, the Cartesian coordinates of each point $p \in R_{ellipse}$ are calculated as:

$$x = a \sin(i \times (\pi / \phi)) \cos(j \times (2\pi / \theta)) \quad (3.1)$$

$$y = b \sin(i \times (\pi / \phi)) \sin(j \times (2\pi / \theta)) \quad (3.2)$$

$$z = c \cos(i \times (\pi / \phi)) \quad (3.3)$$

where a and b are the equatorial radii along the x- and y-axis respectively, and c is the polar radius along the z-axis. They are calculated as:

$$a = (x_1 - x_2) / 2 \quad (3.4)$$

$$b = (y_1 - y_2) / 2 \quad (3.5)$$

$$c = (z_1 - z_2) / 2 \quad (3.6)$$

ϕ is the colatitude or zenith which controls the number of x-y planes, and θ is the longitude in 2π or azimuth which controls the number of points in each x-y plane such that $0 \leq \phi \leq \pi$ and $0 \leq \theta \leq 2\pi$.

Clearly the selection of ϕ and θ values are critical: too few points do not produce a meaningful contour while too many result in excessive computation. We have developed an optimal approach to calculate the two optimal values ϕ_{opt} and θ_{opt} . First, let Φ and Θ be the sets of pre-defined zenith and azimuth values respectively such that:

$$\forall \phi \in \Phi, \frac{\pi}{\phi} \in Z \quad (4.1)$$

$$\forall \theta \in \Theta, \frac{2\pi}{\theta} \in Z \quad (4.2)$$

Next, exhaustively calculate the distances d_1 and d_2 for every combination of ϕ and θ such that:

$$d_1 = |p_0 - p_1| \quad (4.3)$$

$$d_2 = |p_1 - p_2| \quad (4.4)$$

where $p_0 = p_{\theta=i}^{\phi=i}$, $p_1 = p_{\theta=i}^{\phi=i+1}$ and $p_2 = p_{\theta=i+1}^{\phi=i+1}$; ϕ_{opt} and θ_{opt} are obtained when $|d_1 - d_2|$ is minimal.

Without further processing, the current set of ellipsoidal contour points has the limitation that as $i \times (\pi / \theta)$ approaches $\pi / 2$, the distance between adjacent points with the same $i \times (\pi / \phi)$ value but different $j \times (2\pi / \theta)$ value grows unacceptably. Furthermore, the resulting 3D mesh is not suitable for subsequent 3D active contouring. To counter this, we have developed the following technique to produce a 3D mesh consisting of the following set of points:

$$R_{snake} : R_{snake} \supseteq R_{ellipse} \quad (5.1)$$

in which the triangular strips are permuted in a Freudenthal triangulation-like fashion. Using equations (3.1) to (3.6) and ϕ_{opt} and θ_{opt} , for $p_1, p_2 \in R$ let

$p_1 = p_{j=0}^{i=1}$ and $p_2 = p_{j=1}^{i=1}$ and calculate base distance \bar{d} as:

$$\bar{d} = |p_1 - p_2| \quad (5.2)$$

Next, for all subsequent points $p_m = p_{j=1 \dots (\pi / \phi) - 1}^{i=0 \dots (\pi / \phi)}$ and $p_n = p_{l=j+1}^{k=i}$ calculate the distance using (5.2) and where it is $\geq 2\bar{d}$, insert additional points such that the resulting distances between the new points are $\leq \bar{d}$.

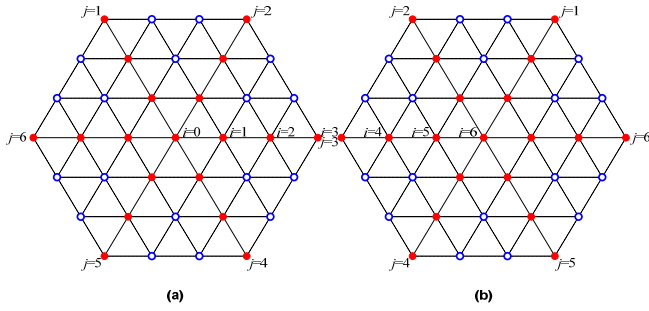


Fig. 2 (a) front view and (b) back view of a sample 3D ROI mesh with $\phi = \frac{1}{6}\pi$ and $\theta = \frac{1}{6}2\pi$. Solid red dots are the initial ellipsoidal contour points and the blue hollow dots are the added contour points.

That is, given $\delta = (\pi/\phi) + 1$ corresponds to the number of x-y planes, the number of points per x-y plane λ_i can be calculated where $\forall i = 0 \dots (\delta - 1)$, $\lambda_0 = \lambda_{\delta-1} = 1$ and $\delta \geq 5$:

if δ is odd:

$$\lambda_i = (2\lambda/\theta) \times i : \forall i = 1 \dots ((\delta - 1)/2) \quad (5.3)$$

$$\lambda_i = (2\lambda/\theta) \times ((\delta - 1) - i) : \forall i = ((\delta + 1)/2) \dots (\delta - 2) \quad (5.4)$$

if δ is even:

$$\lambda_i = (2\lambda/\theta) \times i : \forall i = 1 \dots (\delta - 2)/2 \quad (5.5)$$

$$\lambda_i = (2\lambda/\theta) \times ((\delta - 1) - i) : \forall i = (\delta/2) \dots (\delta - 2) \quad (5.6)$$

A minimum of five x-y planes is chosen as anything lower does not produce a 3D mesh fit for our purpose. See Fig. 2 for illustration.

C. 3D Snake

The basic snake equation is as follows:

$$\varepsilon = \int (\alpha(s)E_{cont} + \beta(s)E_{curv} + \gamma(s)E_{img}) ds \quad (6)$$

where E_{cont} , E_{curv} and E_{img} represent the energy for the continuity, smoothness and edge attraction of the active contours respectively, while the three parameters α , β and γ control the sensitivity of each corresponding property. In the discrete case where the contour is replaced by a chain of N snake points p_1, p_2, \dots, p_N , the

equation becomes:

$$\varepsilon = \sum_{i=1}^N \alpha \times E_{cont}^i + \beta \times E_{curv}^i + \gamma \times E_{img}^i \quad (7)$$

where the three energy terms are:

$$E_{cont}^i = (\bar{d} - \|p_i - p_{i-1}\|)^2 \quad (7.1)$$

$$E_{curv}^i = \|p_{i-1} - 2p_i + p_{i+1}\|^2 \quad (7.2)$$

$$E_{img}^i = -\|\nabla I\| \quad (7.3)$$

and \bar{d} equals the average distance between the pairs (p_i, p_{i-1}) and ∇I is the spatial gradient of the intensity image I , computed at each point.

We have chosen to implement the greedy algorithm for its simplicity and low computational complexity [39]. A $3 \times 3 \times 3$ cubic window centred at each snake point is defined within which the energy functions are locally minimised. Although a $5 \times 5 \times 5$ cubic window was also tested, it was disregarded due to incurrence of almost twice the processing time without noticeable improvement in delineation accuracy. Next, instead of having only the two pre- or post-neighbouring points in the planar setting, a $n \times m$ matrix M_m^n is constructed where n is the number of points in R_{snake} and m is the number of neighbouring snake points such that $m \leq (2\pi/\theta)$. Given again $\delta = (\pi/\phi) + 1$ corresponds to the number of x-y planes, the number of points per x-y plane λ_i can be calculated as follows:

$$\forall i = 0 \dots (\delta - 1), m_0 = m_{\delta-1} = (2\pi/\theta) \text{ and } \delta \geq 5 :$$

if δ is odd:

$$m_i = 6 : \begin{cases} \forall i = 1 \dots (((\delta - 1)/2) - 1) \\ \forall i = ((\delta + 1)/2) \dots (\delta - 2) \end{cases} \quad (8.1)$$

$$m_i = 4 : i = (\delta - 1)/2 \quad (8.2)$$

if δ is even:

$$m_i = 6 : \begin{cases} \forall i = 1 \dots ((\delta - 2)/2) - 1 \\ \forall i = ((\delta/2) + 1) \dots (\delta - 2) \end{cases} \quad (8.3)$$

$$m_i = 5 : \forall i = ((\delta/2) - 1) \dots (\delta/2) \quad (8.4)$$

See Fig. 3 for illustration.

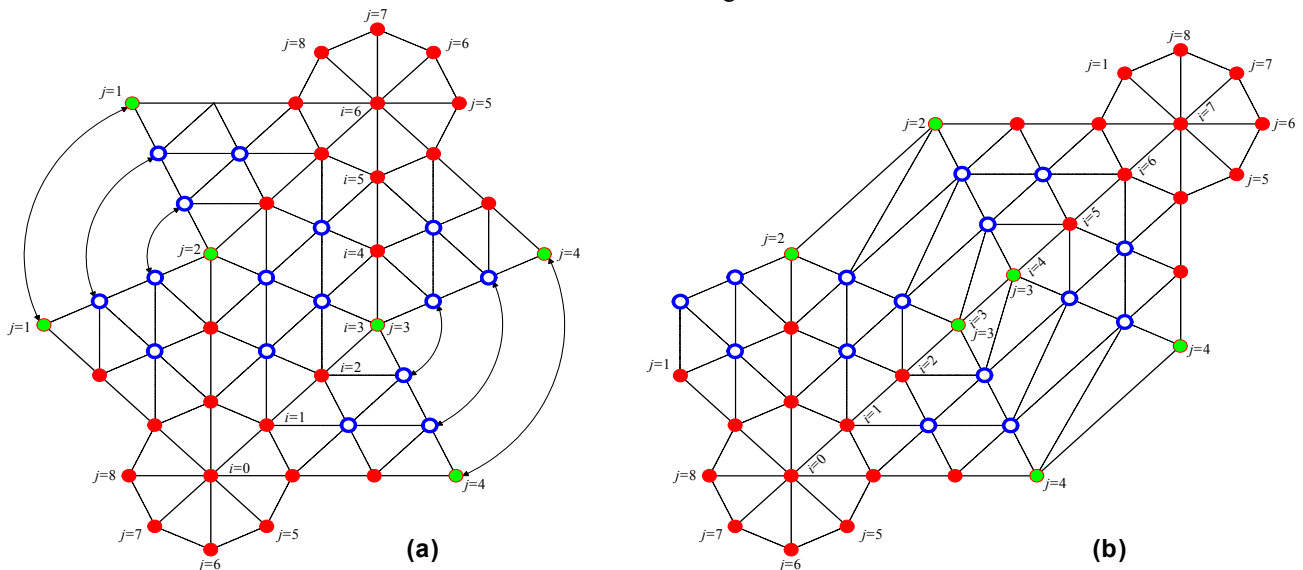


Fig. 3 Sample 3D ROI mesh with $\theta = \frac{1}{8}2\pi$. For solid red dots and blue hollow dots, the number of neighbouring points $m = 6$, whereas the green solid dots are special edge points with $m = 4$ when (a) δ is odd, and $m = 5$ when (b) δ is even.

As this is a 3D implementation of planar active contours, we now refer to the three energy terms as surface continuity, surface smoothness, and surface attraction. While the surface attraction energy term E_{img}^i remains the same for each snake point, the continuity and smooth surface energy terms have to be modified to cater for the 3D snake. To obtain E_{img}^i , our previous approach was to create a gradient image cube by performing planar Gaussian smoothing and Sobel edge detection each image slice [11]. In order to make our method truly 3D in all aspects, we apply the following 3D Gaussian filter and Sobel kernels at each iteration I_n :

$$G_{x,y,z} = \frac{1}{(2\pi\sqrt{2\pi})^3} e^{-\frac{x^2+y^2+z^2}{2\sigma^2}} \quad (9)$$

$$S\{\{-1,0,1\}, \{-1,0,1\}, \{-1,0,1\}\} := \quad (10)$$

$$\left\{ \begin{array}{l} \left[\begin{array}{ccc} 1 & 0 & -1 \\ 2 & 0 & -2 \\ 1 & 0 & -1 \end{array} \right], \left[\begin{array}{ccc} 2 & 0 & -2 \\ 4 & 0 & -4 \\ 2 & 0 & -2 \end{array} \right], \left[\begin{array}{ccc} 1 & 0 & -1 \\ 2 & 0 & -2 \\ 1 & 0 & -1 \end{array} \right], \\ \left[\begin{array}{ccc} 1 & 2 & 1 \\ 0 & 0 & 0 \\ -1 & -2 & -1 \end{array} \right], \left[\begin{array}{ccc} 2 & 4 & 2 \\ 0 & 0 & 0 \\ -2 & -4 & -2 \end{array} \right], \left[\begin{array}{ccc} 1 & 2 & 1 \\ 0 & 0 & 0 \\ -1 & -2 & -1 \end{array} \right], \\ \left[\begin{array}{ccc} 1 & 2 & 1 \\ 2 & 4 & 2 \\ 1 & 2 & 1 \end{array} \right], \left[\begin{array}{ccc} 0 & 0 & 0 \\ 0 & 0 & 0 \\ 0 & 0 & 0 \end{array} \right], \left[\begin{array}{ccc} -1 & -2 & -1 \\ -2 & -4 & -2 \\ -1 & -2 & -1 \end{array} \right] \end{array} \right\}$$

Next, with the surface continuity energy term E_{cont}^i specified in (7.1), note that the average distance \bar{d} does not refer to the overall average distance between all snake points and their corresponding neighbouring points as in planar active contouring; it only refers to the average distance between the current snake point and its neighbouring points in a 3D context. That is, the equation now becomes:

$$E_{cont}^i = \sum_{j=1}^m (\bar{d}_i - \|p_i - M_j^i\|)^2 \quad (11.1)$$

$$\bar{d}_i = \frac{\sum_{j=1}^m \|p_i - M_j^i\|}{m} \quad (11.2)$$

Finally, for the planar smoothness energy term E_{curv}^i specified in (7.2), instead of calculating the squared sum of the distances between a snake point and its immediate pre- or post-neighbouring points, the sum of the squared distances between each snake point and all of its neighbouring points is calculated for surface smoothness. That is, the equation now becomes:

$$E_{curv}^i = \sum_{j=1}^m (p_i - M_j^i)^2 \quad (12)$$

Based on the changes above, Equation (7) can be written as:

$$\varepsilon = \sum_{i=1}^n \sum_{j=1}^m \alpha \times \left(\frac{\sum_{j=1}^m \|p_i - M_j^i\|}{m} - \|p_i - M_j^i\| \right)^2 + \beta \times (p_i - M_j^i)^2 + \gamma \times \|\nabla I\| \quad (13)$$

Note however, in order to correctly implement the greedy 3D active contours algorithm above, it is crucial to normalise the contribution of each energy term. For each snake point p_i , the normalised surface continuity and surface smoothness terms $^{norm}E_{cont}^i$ and $^{norm}E_{curv}^i$ can be calculated by dividing the corresponding maximum value in the $w \times w \times w$ cubic window in which p_i moves; that is:

$$^{norm}E_{cont}^i = \frac{E_{cont}^i}{\max E_{cont}^i} \quad (14.1)$$

$$^{norm}E_{curv}^i = \frac{E_{curv}^i}{\max E_{curv}^i} \quad (14.2)$$

The surface attraction energy should also be normalised by the norm of the spatial gradient, thus becoming:

$$^{norm}E_{img}^i = \frac{-\|\nabla I\| - \min E_{img}^i}{\max E_{img}^i - \min E_{img}^i} \quad (14.3)$$

Based on the findings from our previous study, we continue to use the parameter settings of $\alpha = 1$, $\beta = 1$ and $\gamma = 0.75$ after comparing our delineated contours against those visually delineated by experienced physicians. To prevent the algorithm from entering an endless loop, two constraints have been put in place. First, the number of iterations I is less than or equal to 100. Next, the % change in overall average distance between snake points $\Delta \tilde{d}$ must be less than or equal to 0.1% such that $\forall a = 1 \dots I$:

$$\Delta \tilde{d} = \frac{\|\tilde{d}_a - \tilde{d}_{a-1}\|}{\max(\tilde{d}_a, \tilde{d}_{a-1})} \quad (15.1)$$

$$\tilde{d} = \frac{\sum_{i=1}^n \sum_{j=1}^m \|p_i - M_j^i\|}{m \times n} \quad (15.2)$$

The two constraining values have been chosen after evaluating the results obtained from the entire dataset.

D. Hotspot Simulations

The need for known-volume simulations with artificially introduced defects has been identified in our previous studies. One such defect of significance is hotspots. We propose the following novel approach to generate a set of 30 simulations defected by artificially simulated hotspots. First, 30 base simulations with varying MCV/TCV are chosen. Next, randomly choose the number of hotspots H_n to be simulated, the radius of each hotspot H_r in voxels, and the multiplication factor of each hotspot H_m such that $1 \leq H_n, H_r \leq 5$ and $H_m := \{1.2, 1.4, 1.6, 1.8, 2.0\}$.

Table 1 Statistical agreement results for the set of simulated hotspots.

	$D_{\mu}^{1..30}$	$D_{\sigma}^{1..30}$
$\mu - 2\sigma$	-4.20%	-8.62%
μ	-1.55%	-3.12%
$\mu + 2\sigma$	1.10%	2.38%

The ranges are chosen based on characteristics of the hotspots observed in the subject dataset. For every hotspot, randomly select its origin such that its volume contains non-zero lung voxels, and calculate the mean value \bar{h} . According to Central Limit Theorem, which states that the sum of random numbers becomes normally distributed as more and more of the random numbers are added [40], the value of each hotspot point is calculated as:

$$h_i = \bar{h} \times H_m + \sqrt{\bar{h}} \times \left(\left(\sum_{j=1}^{12} a \right) - 6 \right) \quad (16)$$

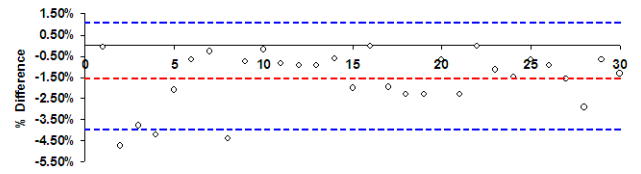
where a is a randomly generated number such that $0.0 \leq a < 1$. To simulate SPECT image transformation, the hotspot is then blurred with a 12mm FWHM Gaussian filter, which is equivalent to a 3-1-3 Gaussian filter also implemented in 3D using equation (9). Finally, the result is added to the selected base simulation above, turning it into a simulation with artificially generated and inserted hotspot.

IV. IMPLEMENTATION AND RESULTS

A. Hotspot Simulations

Without the construction of a hotspot-filled phantom and quantitative measures of hotspots in the real subject SPECT scans, it is impossible to perform accurate numerical comparisons for the hotspots simulated. However, given our goal is not to accurately quantify the hotspots and/or remove them for subsequent PE analysis, but rather to incorporate the high MCV created by their existence, validation will be carried out via visual inspections and quantitative analysis on their statistical impact on the underlying simulation.

Upon examination by experienced physicians, although the shapes of the simulated hotspots are generally spherical with occasional deformation due to overlapping of multiple hotspots, it is agreed that the varying degree of hotspot magnitude, location and size are of more importance. Based on this assertion, our set of hotspot-infected simulations are



(a)



(b)

Fig. 4 Bland-Altman graphs on the agreements between the set of 30 simulations before and after hotspot insertions in terms of (a) mean and (b) standard deviation. The red dash line represents the μ , and the two blue dash lines represent the limits of $\mu \pm 2\sigma$ respectively.

visually satisfactory. The main concern revolves around the impact these simulated hotspots have on the underlying set of simulations that have been statistically verified. First, the means and standard deviations for the set of 30 hotspot-free base simulations are defined as $\mu_B^{1..30}$ and $\sigma_B^{1..30}$.

Similarly, the same statistical measures for the same base simulation set post hotspot insertion are defined as $\mu_H^{1..30}$ and $\sigma_H^{1..30}$. Next, to assess the degree of agreement between the two simulation sets, Bland-Altman graph is utilised to avoid misinterpretation of using these statistical measures alone [41]. Hence, the corresponding sets of differences $D_{\mu}^{1..30}$ and $D_{\sigma}^{1..30}$ represented as percentages are calculated such that $\forall i = 1 \dots 30$:

$$D_{\mu}^i = \frac{\mu_B^i - \mu_H^i}{\mu_B^i} \quad (17.1)$$

$$D_{\sigma}^i = \frac{\sigma_B^i - \sigma_H^i}{\sigma_B^i} \quad (17.2)$$

To plot the graphs, the μ and $\mu \pm 2\sigma$ values for each difference set are also calculated where $\mu \pm 2\sigma$ represent 95% confidence level under normal distribution. See Table 1 and Fig. 4 for Bland-Altman results and Fig. 5 for sample illustration. Based on the results, only two hotspot-infected simulations should be excluded from the dataset. However, upon close examination, both simulations contain five hotspots (the maximum number allowed as specified

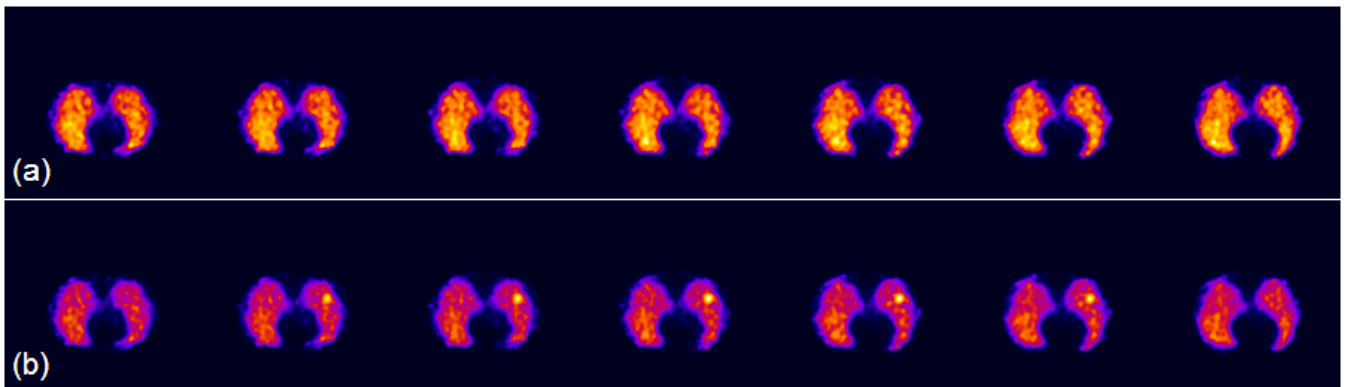


Fig. 5 Sample simulation of a set of extracted sequential slices of (a) the original hotspot free simulation, and (b) after inserting a single simulated hotspot with $h\beta = 3$ and $h\gamma = 1.6$. Note in (b), the visualisation is automatically adjusted to the MCV of the hotspot

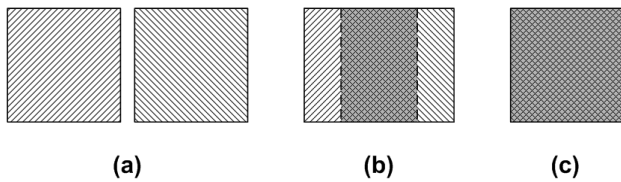


Fig. 6 Illustration of (a) 0%, (b) 50%, and (c) 100% congruency.

previously) each sized at a radius exceeding three voxels. These two simulations are thus kept as good test samples for extreme hotspot-infected cases.

B. Simulation Dataset

To ensure validity and comparability of our results, we use the same measure of congruency C expressed in percentages previously used in our studies as below:

$$C = \frac{V_d \cap V_b}{V_d \cup V_b} \quad (18)$$

where V_d is the delineated volume and V_b is the base volume to which it is compared; 0% means no match whereas 100% represents a perfect match. See Fig. 6 for illustration. This is performed for each image pair (i.e., the base and the delineated), and the corresponding μ and $\mu \pm 2\sigma$ values for the entire set are then calculated for visualisation via Bland-Altman graphs when desired. Given our validation is mainly based on the usage of mean and standard deviation of a dataset's level of agreement measured in percentages, the results will be presented in the form of mean : standard deviation, e.g., 100:0% means perfect agreement.

We evaluate our 3D snake against three sets of simulations: (1) 90 simulations with low MCV/TCV, (2) 50 simulations with normal MCV/TCV, and (3) 30 simulations with high MCV due to artificially inserted hotspots. See Table 2a for results. The first two datasets have been used

previously in our studies to maintain comparability of our results. Given the phantom has a known volume of 61,660 voxels, this is set as the base volume V_b . C is then calculated with V_d equal to the volume delineated by our current method. An average agreement of 96:2% was obtained for the set of 50 normal simulations. In our previous study where DUET alone was used, both the automated method and visual delineation by experienced physician yielded similar agreements that averaged around 97:3%. With the set of 90 low MCV/TCV simulations, our current method achieved an average agreement of 90:9%, which represent a significant increase when compared against the 78:23% and 82:11% achieved by DUET alone and physicians' visual inspection respectively, and marginal increases against 88:8% and 85:9% obtained by our previous methods of planar snake and partial 3D snake respectively. Finally, with the set of 30 hotspot-infected simulations, since our methods rely on DUET as the preliminary means of removing background noise, we first validate its effectiveness. While V_b remain unchanged at 61,660 voxels, V_d now refers to the volume delineated by DUET alone. The results are satisfactorily maintained at 97:3% on average, similar to that achieved with the set of normal simulations. We then validated our current 3D snake method and averaged at a slightly lower agreement of 96:2%.

C. Real Subject Dataset

Having validated the accuracy of our 3D snake method in delineating known-volume simulations with normal and extreme MCV/TCV, we now move on to evaluating its performance against real subject sets. The same two sets of 50 with normal MCV/TCV and 35 with low MCV/TCV previously used to validate our DUET and planar snake methods are recycled See Table 2c for results. As information on the actual lung volumes of the subject scans

Table 2 Volumetric agreement results for three sets of simulations in terms of (a) percentages and (b) number of voxels, and (c) three sets of subject SPECT scans in terms of percentages.

(a)	SET 1					SET 2				SET 3		
	Method A	Method B	Method C	Method D	Method E	Method A	Method C	Method D	Method E	Method A	Method D	Method E
$\mu - 2\sigma$	31.79%	72.76%	67.08%	71.98%	60.64%	92.48%	87.29%	91.54%	92.07%	92.34%	92.62%	89.29%
μ	78.00%	88.19%	85.08%	89.83%	81.81%	97.44%	93.83%	96.16%	96.99%	97.37%	96.93%	95.60%
σ	23.11%	7.71%	9.00%	8.92%	10.58%	2.48%	3.27%	2.31%	2.46%	2.51%	2.15%	3.16%
$\mu + 2\sigma$	124.21%	103.61%	103.07%	107.67%	102.97%	102.40%	100.36%	100.78%	101.91%	102.39%	101.23%	101.91%

(b)	SET 1					SET 2				SET 3		
	Method A	Method B	Method C	Method D	Method E	Method A	Method C	Method D	Method E	Method A	Method D	Method E
$\mu - 2\sigma$	28,044	46,646	43,968	46,167	57,948	57,862	54,084	55,829	58,377	58,041	57,856	54,963
μ	51,954	54,932	53,290	55,954	74,475	62,194	58,040	59,913	62,764	62,389	62,380	59,261
σ	11,955	4,143	4,661	4,894	8,263	2,166	1,978	2,042	2,194	2,174	2,262	2,149
$\mu + 2\sigma$	75,864	63,219	62,611	65,741	91,001	66,525	61,997	63,996	67,152	66,738	66,903	63,558

(c)	SET 4			SET 5			SET 6	
	Method B	Method C	Method D	Method A	Method C	Method D	Method A	Method D
$\mu - 2\sigma$	84.45%	90.24%	90.96%	91.27%	85.43%	87.40%	90.87%	85.95%
μ	95.00%	93.62%	95.15%	96.34%	90.88%	92.85%	96.37%	92.33%
σ	5.27%	1.69%	2.09%	2.53%	2.72%	2.73%	2.75%	3.19%
$\mu + 2\sigma$	105.54%	97.00%	99.33%	101.41%	96.32%	98.31%	101.87%	98.70%

KEY

- SET 1: 90 simulations with low MCV/TCV
- SET 2: 50 simulations with normal MCV/TCV
- SET 3: 30 simulations with hotspots
- SET 4: 35 subject scans with low MCV/TCV
- SET 5: 50 subject scans with normal MCV/TCV
- SET 6: 25 subject scans with hotspots
- Method A: DUET
- Method B: DUET with planar snake
- Method C: DUET with partial 3D snake
- Method D: DUET with full 3D snake
- Method E: Experienced physicians

are not available, volumes qualitatively delineated by experienced physicians will be used as the base of comparison. This is supported by our previously validated results of physicians' ability to achieve 97:2.5% and 82:11%, agreements against the sets of 50 normal simulations and 90 low-count simulations respectively. That is, while V_d remains as the volume delineated by our current method, V_b is now represented by practitioner delineated volumes. For the set of 50 normal SPECT scans, we achieved an excellent average agreement of 95:2% representing a marginal increase against the 95:5% and 94:2% mean congruencies achieved by our previous methods of planar snake and partial 3D snake respectively. For the set of 35 low-count SPECT scans, we achieved 93:3% average agreement indicating improvement against the 91:3% achieved by partial 3D snake; however, performance degradation is observed when comparing against the 96:3% achieved by DUET alone. For evaluation of the accuracy of our method on delineating lung volumes of real subject SPECT scans with hotspots, a set of 25 scans with clearly visible hotspots located at various locations in the lungs is chosen by the physicians and delineated visually. Before using the set of visually delineated volumes as the base of comparison, the physicians are called upon to visually delineate the set of 30 hotspot-infected simulations in order to validate the reliability of their delineation ability; an average agreement of 96:3% indicated positive outcomes. Furthermore, the accuracy of DUET alone in removing background noise is also confirmed with mean congruency of 96:3%. Finally, by comparing volumes delineated by our 3D snake method against those of the physicians, we achieved yet another highly satisfactory agreement of 92:3% on average.

V. DISCUSSION

A. Main Findings

In this paper, we have shown that the combination of DUET with 3D active contours continue to deliver an overall congruency of 90% when comparing the delineated volumes against known-volume simulations and subjects visually delineated by practitioners. We have also developed a quick method for inserting artificial hotspots into existing Monte Carlo simulations without impacting their underlying Poisson distribution characteristics or creating additional phantoms.

With low-count subject scans, while our current 3D snake method has achieved similar mean average of 95% when

compared against our previous planar snake method, 3D snake is producing more consistent results indicated by the lower variance of 2% standard deviation rather than the old 5%. It has also improved upon the limitation of over delineation evident in our previous partial 3D snake method with a marginal increase of 1.5:0.5% in agreement. The results are also consistent when compared against those obtained via validation of known-volume simulations with low MCV/TCV. For normal subject scans, the high 96:3% mean agreement indicate that DUET alone has better performance than coupling it with partial/full 3D snake, a result that is consistent with the 97:2.5% obtained via simulation validation. As the base volumes for evaluating subject scans are those delineated by experienced practitioners, their ability to delineate known-volume simulations up to the similar 97:2.5% benchmark further confirms reliableness of these results. Finally, in terms of subject scans containing hotspots, our fully 3D snake method has maintained its ability to delineate SPECT lung volumes with high accuracy of 92:3% mean agreement despite an approximate performance degradation of 4:0.5% on average. This is also backed by results validated against known-volume simulations. See Fig. 7 for illustration.

It is evident that although our true 3D snake method has yielded excellent results for SPECT scans with different MCV/TCV, it is especially useful when delineating low-count scans while being outperformed slightly by DUET alone when delineating normal- to high-count scans. Given the lack of information on the actual lung volumes of the subject scans and the fact that this trend was also observed in the corresponding simulation sets, quantitative analysis is performed on the known-volume simulations to identify potential limitations of our method. Upon closer examination of the delineated lung contours for normal and hotspot-infected simulations, it was found that the decrease in congruency was due to overall marginal decreases in the delineated volumes. While post-DUET lung volumes for both normal and hotspot-infected simulations remain around 62,200 voxels, subsequent application of 3D snake decreased the volumes by about 4% to 59,913 voxels on average in the former set, and a negligible 0.015% in the latter set. See Table 2b for results. This indicates that 3D snake has either successfully removed false lung tissues and/or background noise that are not visually recognisable, or has over-aggressively removed true lung regions. Given the known phantom volume of 61,660 voxels, this concludes the 3D snake method to be slightly over-aggressive causing removal of true lung tissues. See Fig. 8 for illustration.

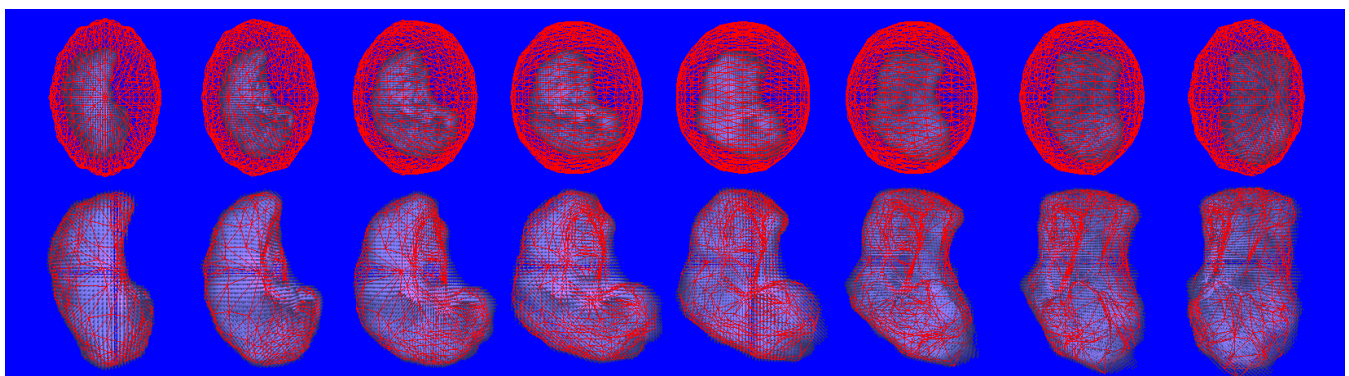


Fig. 7 Sample SPECT lung delineation of a left lung with the top row showing the initial starting ROI ($\phi = 10$ and $\theta = 30$) encasing the post dual exponential threshold lung, and the bottom row showing the final delineation after 3D active contours.

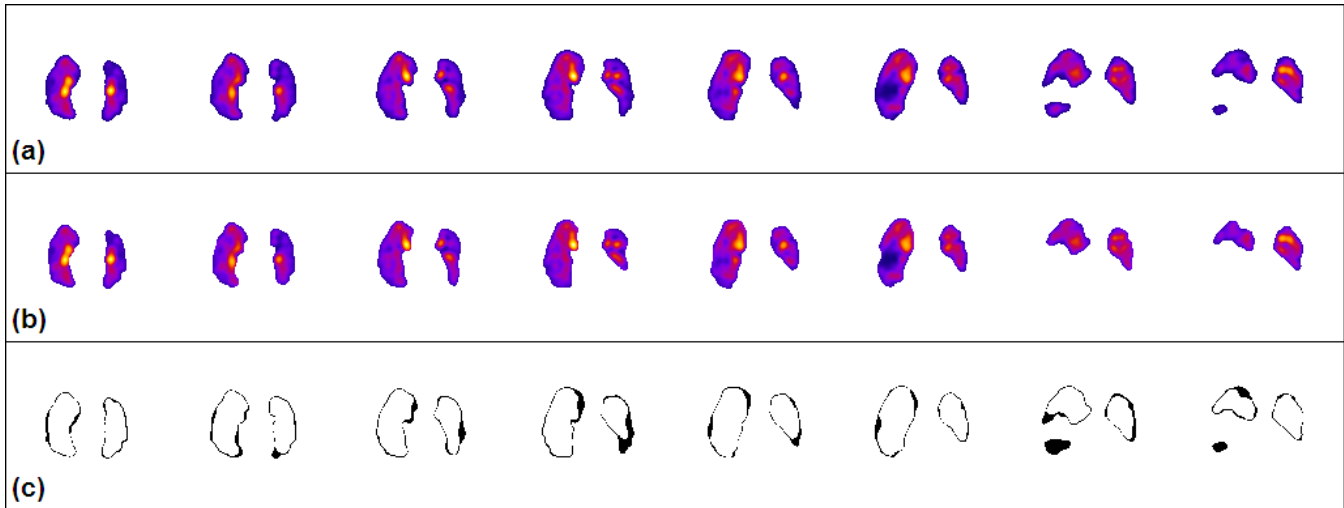


Fig. 8 Sample delineation of a subject SPECT scan with hotspots in the hilum region using (a) DUET alone and (b) full 3D snake. The difference between the two methods is illustrated in (c).

B. Future Work

Based on the results, it is clear that future work is required to identify the cause of the 3D snake's over-aggressiveness in contour delineation. However, examination of Fig. 8 yields some clues in that the method attracts the contour towards the hotspot outlines where the gradient difference is higher, and smaller regions with less prominent voxel values are excluded due to current method's limitation in segmenting multiple objects – both leading to the removal of true lung tissues. Hence, immediate improvement can be made by incorporating segmentation of multiple objects as well as reducing the method's sensitivity towards hotspot edges. Furthermore, ways of adjusting the snake's parameters dynamically may be developed and/or additional energy term(s) introduced to specifically cater for full 3D implementation. From a dataset perspective, although we have developed methods for mass generating simulations and hotspots quickly based on an original set obtained from a single phantom study, additional phantoms that contain defect(s) similar to those seen in subject scans with "hotspots" and/or irregular contours induced by other cardiopulmonary disorders are also desirable.

VI. CONCLUSION

To date, although SPECT-CT hybrid machines are available with supporting studies performed on extracting lung contours based on the anatomical information provided by CT, high total costs is still an impeding factor on the installation and usage on a wide scale [42-45]. Based on this notion, we have successfully developed a hybrid method of dynamic thresholding and 3D active contours in delineating SPECT lung contours for PE diagnosis and the detection of other cardiopulmonary disorders. While evaluation against our previous methods of DUET alone and subsequent coupling with planar snake and partial 3D snake on normal-to high-count Monte Carlo simulations and real subject scans revealed marginal delineation of true lung tissues, overall congruency is still above 90%. The method is most useful in delineating low-count subject SPECT scans with 95% agreement on average. Overall, the method detailed in this study provides an accurate and solid foundation for true 3D SPECT lung delineation.

ACKNOWLEDGMENT

We would like to thank the physicians and staff at the Royal North Shore Hospital, Australia for the provision of original datasets and medical guidance.

REFERENCES

- [1] T. M. Morell, "Pulmonary embolism," *British Medical Journal*, vol. 2, pp. 579-584, 1963.
- [2] J. J. Cross, P. M. Kemp, C. G. Walsh et al., "A randomized trial of spiral CT and ventilation perfusion scintigraphy for the diagnosis of pulmonary embolism," *Clinical Radiology*, vol. 53, no. 3, pp. 177-82, 1998.
- [3] D. M. Howarth, L. Lan, P. A. Thomas et al., "99mTc technegas ventilation and perfusion lung scintigraphy for the diagnosis of pulmonary embolus," *Journal of Nuclear Medicine*, vol. 40, no. 4, pp. 579-84, 1999.
- [4] A. Gottschalk, H. D. Sostman, R. E. Coleman et al., "Ventilation-perfusion scintigraphy in the PIOPED study. Part I. Data collection and tabulation," *Journal of Nuclear Medicine*, vol. 37, no. 7, pp. 1109-1118, 1993.
- [5] A. Gottschalk, H. D. Sostman, R. E. Coleman et al., "Ventilation-perfusion scintigraphy in the PIOPED study. Part II. Evaluation of the scintigraphic criteria and interpretations," *Journal of Nuclear Medicine*, vol. 34, no. 7, pp. 1119-1126, 1993.
- [6] M. Bajc, U. Bitzen, B. Olsson et al., "Lung ventilation/perfusion SPECT in the artificially embolized pig," *J Nucl Med*, vol. 43, no. 5, pp. 640-7, 2002.
- [7] M. Bajc, C. Olsson, B. Olsson et al., "Diagnostic evaluation of planar and tomographic ventilation/perfusion lung images in patients with suspected pulmonary emboli," *Clin Physiol Funct Imaging*, vol. 24, pp. 249-256, 2004.
- [8] J. Palmer, U. Bitzen, B. Jonson et al., "Comprehensive ventilation/perfusion SPECT," *J Nucl Med*, vol. 42, no. 8, pp. 1288-94, 2001.
- [9] A. Wang, and H. Yan, "A new automated lung delineation method for SPECT PE diagnosis using adaptive dual exponential thresholding," *Intl J Imaging Sys Tech*, vol. 17, no. 1, pp. 22-27, 2007.
- [10] A. Wang, and H. Yan, "Delineating low-count defective-contour SPECT lung scans for PE diagnosis using adaptive dual exponential thresholding and active contours," *Intl J Imaging Sys Tech*, vol. 20, no. 2, pp. 149-154, 2010.
- [11] A. Wang, and H. Yan, "Delineating SPECT lung contours using 3D snake," *Lecture Notes in Engineering and Computer Science: Proceedings of The International MultiConference of Engineers and Computer Scientists 2010, IMECS 2010, 17-19 March, Hong Kong*, vol. 2, pp. 1494-1499, 2010.
- [12] M. Kass, A. Witkin, and D. Terzopoulos, "Snakes: Active Contour Models," *International Journal of Computer Vision (IJCV)*, vol. 1, no. 4, pp. 321-331, 1988.
- [13] G. An, J. Chen, and Z. Wu, "A fast external force model for

- snake-based image segmentation," 9th International Conference on Signal Processing, pp. 1128-1131, 2008.
- [14] A. K. Mishra, P. Fieguth, and D. A. Clausi, "Accurate boundary localization using dynamic programming on snakes," 2008 Canadian Conference on Computer and Robot Vision, pp. 261-268, 2008.
- [15] M. Sakalli, K. M. Lam, and H. Yan, "A faster converging snake algorithm to local object boundaries," IEEE Transactions on Image Processing, vol. 15, no. 5, pp. 1182-1191, 2006.
- [16] D. J. Williams, and M. Shah, "A fast algorithm for active contours and curvature estimation," CVGIP: Image Understanding, vol. 55, no. 1, pp. 14-26, 1992.
- [17] L. Ji, and H. Yan, "Robust topology-adaptive snakes for image segmentation," 2001 International Conference on Image Processing, vol. 2, pp. 797-800, 2006.
- [18] T. McInerney, and D. Terzopoulos, "Topologically adaptable snakes," 5th International Conference on Computer Vision, pp. 840-845, 1995.
- [19] K. H. Seo, and J. J. Lee, "Object tracking using adaptive color snake model," 2003 International Conference on Advanced Intelligent Mechatronics, vol. 2, pp. 1406-1410, 2003.
- [20] T. F. Chan, and L. A. Vese, "Active contours without edges," IEEE Transactions on Image Processing, vol. 10, no. 2, pp. 266-277, 2001.
- [21] L. D. Cohen, and I. Cohen, "Finite-element methods for active contour models and balloons for 2-D and 3-D images," IEEE Transactions on Pattern Analysis and Machine Intelligence, vol. 15, no. 11, pp. 1131-1147, 1993.
- [22] Y. B. Hou, and Y. Xiao, "Active snake algorithm on the edge detection for gallstone ultrasound images," 9th International Conference on Signal Processing, pp. 474-477, 2008.
- [23] G. Sundaramoorthi, J. D. Jackson, and A. Yezzi, "Tracking with Sobolev Active Contours," 2006 Conference on Computer Vision and Pattern Recognition, vol. 1, pp. 674-680, 2006.
- [24] G. Sundaramoorthi, A. Yezzi, and A. C. Mennucci, "Coarse-to-fine segmentation and tracking using Sobolev active contours," IEEE Transactions on Pattern Analysis and Machine Intelligence, vol. 30, no. 5, pp. 851-864, 2008.
- [25] J. Liang, G. Ding, and Y. Wu, "Segmentation of the left ventricle from cardiac MR images based on radial GVF snake," International Conference on BioMedical Engineering and Informatics, vol. 2, pp. 238-242, 2008.
- [26] H. P. Ng, K. W. C. Foong, S. H. Ong et al., "Medical image segmentation using feature-based GVF snake," 29th Annual International Conference on the IEEE, pp. 800-803, 2007.
- [27] T. Shimada, L. Wang, and M. Saito, "Auto-extraction of brain region from MR image by using snake controlled by neural network," 22nd Annual International Conference of the IEEE, vol. 4, pp. 3177-3179, 2000.
- [28] J. Tang, S. Millington, S. T. Acton et al., "Surface extraction and thickness measurement of the articular cartilage from MR images using directional gradient vector flow snakes," IEEE Transactions on Biomedical Engineering, vol. 53, no. 5, pp. 896-907, 2006.
- [29] W. Wang, L. Ma, and L. Yang, "Liver contour extraction using modified snake with morphological multiscale gradients," International Conference on Computer Science and Software Engineering, vol. 6, pp. 117-120, 2008.
- [30] P. J. Yim, and D. J. Foran, "Volumetry of hepatic metastases in computed tomography using the watershed and active contour algorithms," 16th IEEE Symposium Computer-Based Medical Systems, pp. 329-335, 2003.
- [31] H. Cai, X. Xu, J. Lu et al., "Shape-constrained repulsive snake method to segment and track neurons in 3D microscopy images," 3rd IEEE International Symposium on Biomedical Imaging: Nano to Macro, pp. 538-541, 2006.
- [32] M. Xiao, S. Xia, and S. Wang, "Geometric active contour model with color and intensity priors for medical image segmentation," 27th Annual International Conference of the Engineering in Medicine and Biology Society, pp. 6496-6499, 2005.
- [33] M. Jung, and H. Kim, "Snaking across 3D meshes," 12th Pacific Conference on Computer Graphics and Applications, pp. 87-93, 2004.
- [34] J. Ahlberg, "Active contours in three dimensions," Master Thesis, Linköping University, Sweden, 1996.
- [35] J. S. Magnussen, P. Chicco, A. W. Palmer et al., "Single-photon emission tomography of a computerised model of pulmonary embolism," Eur J Nucl Med, vol. 26, no. 11, pp. 1430-1438, 1999.
- [36] S. Araki, N. Yokoya, H. Iwasa et al., "Splitting of active contour models based on crossing detection for extraction of multiple objects," Systems and Computers in Japan, vol. 28, no. 11, pp. 34-42, 1997.
- [37] C. H. Chuang, and W. N. Lie, "Automatic snake contours for the segmentation of multiple objects," The 2001 IEEE International Symposium on Circuits and Systems, vol. 2, pp. 389-392, 2001.
- [38] T. Srinark, and C. Kambhamettu, "A framework for multiple snakes and its applications," Pattern Recognition, vol. 39, no. 9, pp. 1555-1565, 2006.
- [39] E. Trucco, and A. Verri, Introductory Techniques for 3-D computer vision, 1st ed., New York: Prentice Hall, 1998.
- [40] S. W. Smith, "The Scientist and Engineer's Guide to Digital Signal Processing, 1st Edition," pp. 29-32, 1997.
- [41] J. M. Bland, and D. G. Altman, "Statistical methods for assessing agreement between two methods of clinical measurement," The Lancet, vol. 327, no. 8476, pp. 307-310, 1986.
- [42] B. Harris, D. L. Bailey, P. J. Roach et al., "Fusion imaging of computed tomographic pulmonary angiography and SPECT ventilation/perfusion scintigraphy: initial experience and potential benefit," European Journal of Nuclear Medicine and Molecular Imaging, vol. 34, no. 1, pp. 135-142, 2007.
- [43] P. J. Roach, G. P. Schembri, I. A. Ho Shon et al., "SPECT/CT imaging using a spiral CT scanner for anatomical localization: Impact on diagnostic accuracy and reporter confidence in clinical practice," Nuclear Medicine Communications, vol. 27, no. 12, pp. 977-987, 2006.
- [44] K. Suga, Y. Kawakami, H. Iwanaga et al., "Comprehensive Assessment of Lung CT Attenuation Alteration at Perfusion Defects of Acute Pulmonary Thromboembolism With Breath-Hold SPECT-CT Fusion Images," Journal of Computer Assisted Tomography, vol. 30, no. 1, pp. 83-91, 2006.
- [45] K. Suga, Y. Kawakami, H. Iwanaga et al., "Automated Breath-Hold Perfusion SPECT/CT Fusion Images of the Lungs," American Journal of Roentgenology, vol. 189, no. 2, pp. 455-463, 2007.